Journal of Alloys and Compounds 500 (2010) 61–67

Contents lists available at ScienceDirect

Journal of Alloys and Compounds

journal homepage: www.elsevier.com/locate/jallcom

Effects of severe plastic deformation on the structure and thermo-mechanical properties of $Zr_{55}Cu_{30}Al_{10}Ni_5$ bulk metallic glass

N. Van Steenberge[a,b], S. Hóbor[c], S. Suriñach[a], A. Zhilyaev[d,e], F. Houdellier[f], F. Mompiou[f], M.D. Baró[a], Á. Révész[c], J. Sort[g,*]

[a] Departament de Física, Universitat Autònoma de Barcelona, 08193 Bellaterra, Spain
[b] OCAS, ArcelorMittal Global R&D Gent, BE-9060 Zelzate, Belgium
[c] Department of Materials Physics, Eötvös University, P.O. Box 32, H-1518 Budapest, Hungary
[d] Centro Nacional de Investigaciones Metalúrgicas, 28040 Madrid, Spain
[e] Institute for Metals Superplasticity Problems, RAS, 450001 Ufa, Russia
[f] Centre d'Elaboration de Matériaux et d'Etudes Structurales, CEMES-CNRS, BP 4347, 31055 Toulouse Cedex 4, France
[g] Institució Catalana de Recerca i Estudis Avançats and Departament de Física, Universitat Autònoma de Barcelona, 08193 Bellaterra, Spain

ARTICLE INFO

Article history:
Received 5 February 2010
Received in revised form 21 March 2010
Accepted 25 March 2010
Available online 1 April 2010

Keywords:
Metallic glasses
High pressure
Microstructure
Mechanical properties
Calorimetry
X-ray diffraction

ABSTRACT

Severe plastic deformation induced by high-pressure torsion (HPT) causes significant changes in the microstructure and thermo-mechanical properties of $Zr_{55}Cu_{30}Al_{10}Ni_5$ bulk metallic glass. Although HPT does not directly lead to clear crystallization of the amorphous alloy, transmission electron microscopy reveals changes in the medium-range order. This is accompanied with an increase in the alloy microstrains and a slight decrease in the crystallization enthalpy. These effects are due to the combined action of the large shear strains and the temperature rise that occurs during HPT. Indeed, the time evolution and spatial distribution of temperature during HPT, calculated using a heat-conduction equation, evidence that values of temperature close to the glass transition, T_g, are achieved throughout the HPT disk. However, contrary to conventional sub-T_g thermal annealing, which induces mechanical hardening and embrittlement of the glass, HPT increases the net amount of excess free volume in the amorphous structure, leading to a mechanical softening effect.

1. Introduction

Severe plastic deformation (SPD) techniques are conventionally used to refine the microstructure of crystalline materials to achieve a significant increase of hardness, in accordance with the well-known Hall–Petch relationship [1]. One of the SPD techniques most frequently used for producing bulk nanocrystalline samples is high-pressure torsion (HPT). The HPT method allows obtaining porosity and impurity-free specimens. For example, HPT processing of pure Ni was reported to result in an increase of hardness from 1.4 to 3 GPa while the grain size was reduced from 100 μm to 170 nm [2]. The use of HPT in the processing of metallic glasses is still rather limited. So far, it has been successfully applied as a compacting method for amorphous ribbons, in order to obtain a homogeneous bulk (nanocrystalline) material with improved properties compared to the initial ribbons [3–5]. Very recently, metallic glass was produced by HPT directly from a crystalline ingot, thus surpassing the size-limiting issues of rapid cooling techniques [6]. In some cases, processing of metallic glasses by means of HPT maintains the amorphous structure of the alloy but introduces a large structural anisotropy [7].

The effects of plastic deformation (induced by rolling, bending, nanoindentation or compression) on the microstructure and properties of bulk metallic glasses are, in fact, under discussion [8]. It is generally accepted that plastic flow leads to dilatation (i.e., creation of free volume), an effect which has been characterized by different experimental techniques such as calorimetry, density measurements, synchrotron radiation or positron annihilation [9–12]. Dilatation causes mechanical softening leading, for example, to an indentation size effect [13,14]. Besides dilatation, nanovoids are often observed inside shear bands as a result of coalescence of excess free volume [15,16]. Depending on the glass composition and the applied shear strains, deformation at room temperature can induce a variety of additional microstructural changes, such as nanocrystallization [17–21] phase separation within the amorphous structure [22] or other types of phase transitions [23]. Similar changes have been reported upon deformation at high temperatures [24,25] and even at cryogenic temperatures [26]. In certain cases, these "in situ" microstructural changes are thought to be responsible for the observed improved mechanical behavior

* Corresponding author. Tel.: +34 935811401; fax: +34 935812155.
E-mail address: jordi.sort@uab.es (J. Sort).

0925-8388/$ – see front matter © 2010 Elsevier B.V. All rights reserved.
doi:10.1016/j.jallcom.2010.03.195

(e.g., enhanced plasticity). Furthermore, deformation techniques and HPT in particular introduce an inhomogeneous stress state. These residual stresses have their influence as well on the mechanical response of metallic glasses [27].

The observed deformation-induced nanocrystallization of metallic glasses has been a topic of investigation during the last years. Several factors, such as temperature rise due to localized heating at shear bands, enhanced diffusion induced by the larger amounts of defects (dilatation) or growth of pre-existing nanocrystalline nuclei during deformation, can explain this effect. It should be noted that in addition to the temperature raise [28,29], the shear strain rate also plays an important role on deformation-induced structural changes [30]. Actually, the strain state itself (compression versus tension) appears to be important as well, whereas the temperature rise is expected to be independent of this strain state [31]. Lee et al. ascribed nanocrystallization during uniaxial compression to a decrease in the energy barrier due to the applied stresses. These stress states not only reduce the energy barrier for overall crystallization but can also lower the energy barrier for diffusion. Therefore, compression can enhance the nucleation rate, thus promoting nanocrystallization [20]. Another possibility is that shearing affects not only the kinetics but also the thermodynamics of glass-forming alloys. Short-range chemical and topological ordering might be altered by the non-equilibrium conditions associated with strong shear flow. Since a large portion of the activation barrier for homogeneous nucleation in glass-forming liquids comes from the need to establish compositional fluctuations, chemical ordering may significantly lower the activation barrier for crystallization [8].

In this work, we investigate the changes in microstructure, thermal properties and mechanical behavior of $Zr_{55}Cu_{30}Al_{10}Ni_5$ bulk metallic glass after being processed by HPT. This technique offers the possibility to apply a large amount of deformation, without failure, even in brittle materials like metallic glasses. Although no crystallization occurs in this alloy for the HPT conditions of our experiment, changes in the amount of free volume and medium-range order are evidenced by differential scanning calorimetry and high-resolution transmission electron microscopy, respectively. These microstructural changes result in a softening of the metallic glass, in contrast to the mechanical hardening typically observed after HPT of crystalline materials.

2. Materials and methods

Metallic rods with nominal composition $Zr_{55}Cu_{30}Al_{10}Ni_5$ (at.%) were prepared by injection casting the arc-melted ingots, obtained from high-purity (>99.9%) elements, into a Cu-mould. The rods were cut into pieces and subsequently subjected to $N = 2$ whole-turn torsion under an applied pressure of 6 GPa, using a modified Bridgemann anvil type device. Porosity-free disks with a diameter of $R = 10$ mm and $L = 300$ μm in thickness were obtained. Heat treatments of the initial as-cast rods were also performed under vacuum with Ti as oxygen-getter in a tubular furnace, introducing the samples into a preheated furnace at 623 K (just below the glass transition) and 723 K (below the crystallization temperature). Once the samples reached the desired temperature, they were immediately cooled down, in air, to room temperature.

The amorphous nature of all samples was verified by X-ray diffraction (XRD), using a Philips X'Pert diffractometer with monochromatic Cu Kα radiation. For thermal analysis, a Perkin-Elmer differential scanning calorimeter (DSC-7 model), operating at a heating rate of 0.667 K/s, was employed. Microstructural characterization of as-cast, HPT disk and heat-treated samples was performed using a 200 kV Hitachi 600AB transmission electron microscope (TEM). Samples for TEM observations were mechanically thinned to 30 μm and then further thinned by electropolishing them using a solution of 30% HNO_3 in methanol at a temperature of 253 K. Due caution was taken to maintain the same conditions for the preparation of each sample. Afterwards, ion beam thinning at 2 keV and an incident angle of 4° was applied for a short time. To observe medium-range order within the amorphous structure, a high-resolution transmission electron microscope with a corrector for spherical aberration (C_s-corrected F20-SACTEM Tecnai HRTEM, operating at 200 kV) was employed. Nanoindentation experiments were carried out with an MTS nanoindenter XP, at room temperature, in load control mode using a Berkovich indenter tip. Prior to nanoindentation, the samples were carefully polished to mirror-like appearance using diamond paste. The indentation function consisted of a loading segment of 40 s, followed by a load holding segment of 30 s and an unloading segment of 10 s. The hardness and Young's modulus were calculated using the method of Oliver and Pharr [32], from indentation curves acquired to a maximum load was 250 mN. Proper calibration for the contact area was performed on fused silica specimens. The thermal drift was always kept below $\pm 0.03\ \mathrm{nm\,s^{-1}}$. Lower loads were used to study serrated plastic flow (or pop-in events) during deformation of the metallic glass.

3. Theory and calculation

The thermo-mechanical behavior of the HPT disks can be explained in terms of a three-dimensional thermoplastic model based on heat conduction [33]. In brief, the disk-shape sample with a radius of R and thickness L is placed between two cylindrical stainless steel anvils. The temperature evolution in the disk can be derived from the heat-conduction equation:

$$c(\mathbf{r}) \cdot \rho(\mathbf{r}) \frac{\partial T(\mathbf{r}, t)}{\partial t} - \Delta(k(\mathbf{r}) \cdot T(\mathbf{r}, t)) = S(\mathbf{r}, t) \tag{1}$$

where $c(\mathbf{r})$, $\rho(\mathbf{r})$ and $k(\mathbf{r})$ are the heat capacity, the density and the heat conductivity, respectively. $S(\mathbf{r}, t)$, the plastic deformation-induced heat release, can be calculated as

$$\begin{cases} \beta \cdot \sigma \cdot \dfrac{d\gamma}{dt}, & \text{if } T < T_g \\ \beta \cdot \eta \left(\dfrac{d\gamma}{dt} \right)^2, & \text{if } T > T_g \end{cases} \tag{2}$$

where β, σ, γ and η are, respectively, the fraction of plastic work converted to thermoplastic heating, the yield stress, the shear strain and the viscosity that can be obtained from the Vogel–Fulcher equation [34]. The accumulated shear strain during the HPT process at a radial distance r can be represented by

$$\gamma(r, t) = \frac{2\pi \cdot N \cdot r}{L} = \frac{2\pi \cdot r}{L \cdot t_{rev}} \cdot t \tag{3}$$

where N and t_{rev} are number of rotations and the revolution time (60 s in our case) of the rotating anvils, respectively [35]. Note that the shear strain increases with the radius in a simple linear way at a fixed time and also linearly increases with time at a fixed r. Hence, larger shear strain develops at the edge of the disk during the HPT process. Solving the above equations with proper values of k, c and ρ for the bulk metallic glass [28] and the stainless steel anvils, allows obtaining the evolution of temperature with time, as a function of the disk radius, during the HPT process (see Fig. 1). The figure indicates that the dependence of temperature as a function of time is similar for all r values, just become a bit lower at the edges of the disk due to the thin air layer that surrounds the HPT disk. Actually, after two whole revolutions (120 s) temperature is between 650 and 700 K throughout the compressed disk, thus close to the glass transition (which is 702 K, as will be described in Section 4.1).

4. Results and discussion

4.1. Thermal characterization

Thermal analysis by means of DSC (Fig. 2) shows that SPD preserves the general amorphous character of the initial, undeformed, rod. Both specimens (as-quenched and HPT disks) exhibit an exothermic event, corresponding to thermally induced structural relaxation, and a clear glass transition at $T_g = 702 \pm 1$ K [see inset (a) for details]. Structural relaxation is followed by a crystallization peak. The onset of crystallization occurs at $T_x = 777 \pm 3$ K for both the center and edge of the HPT disk and at $T_x = 780 \pm 3$ K for the as-quenched rod. A slight decrease (≲4%) in crystallization enthalpy, ΔH_x, is observed in the HPT disk ($\Delta H_x = 49 \pm 1$ J/g) as compared to the as-cast sample. Although the difference in crystallization enthalpy between as-quenched and deformed specimens

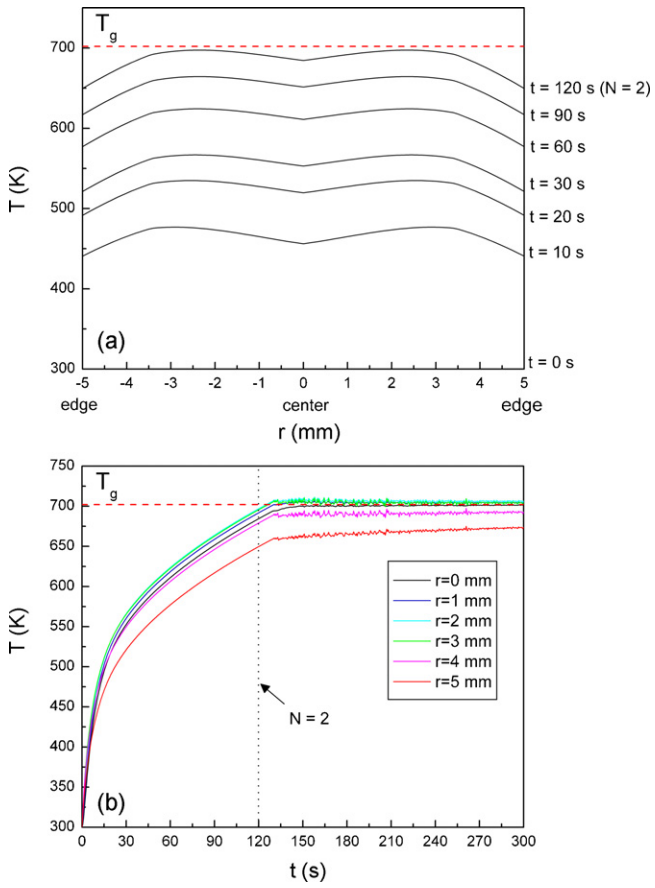

Fig. 1. (a) Temperature profiles, along the disk radius, during the HPT process, obtained from the heat-conduction equation (Eq. (1)); (b) dependence of temperature as a function of processing time during high-pressure torsion (HPT), at different distances from the rotation axis. These temperature profiles were calculated taking into account heat dissipation through the HPT steel anvils. Note that $t = 120$ s corresponds to two whole HPT turns ($N = 2$).

seems negligible, a clear change in the shape of the crystallization peak is observed after HPT [see inset (b)], similar to the broadening observed in the crystallization peak after heating to 623 K, i.e. sub-T_g annealing (see Fig. 3). This is probably due, at least in part, to the temperature raise that accompanies the HPT processing (Fig. 1).

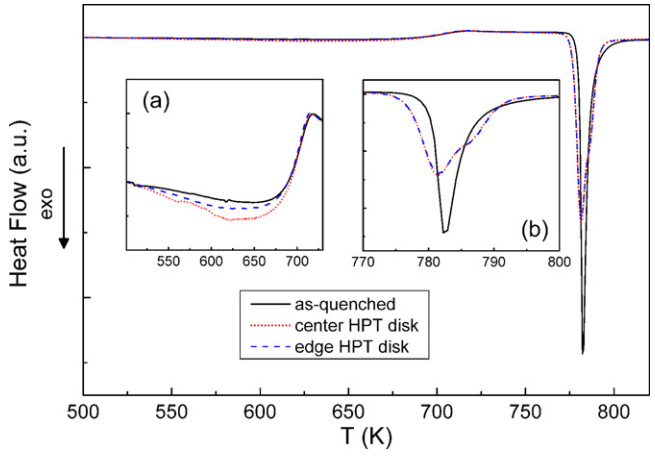

Fig. 2. Differential scanning calorimetry (DSC) curves of the as-quenched $Zr_{55}Cu_{30}Al_{10}Ni_5$ rod and the central and edge portions of a disk processed by high-pressure torsion. Inset (a) is an enlargement of the endothermic halos corresponding to the glass transition regions, while inset (b) is a zoom of the crystallization peaks.

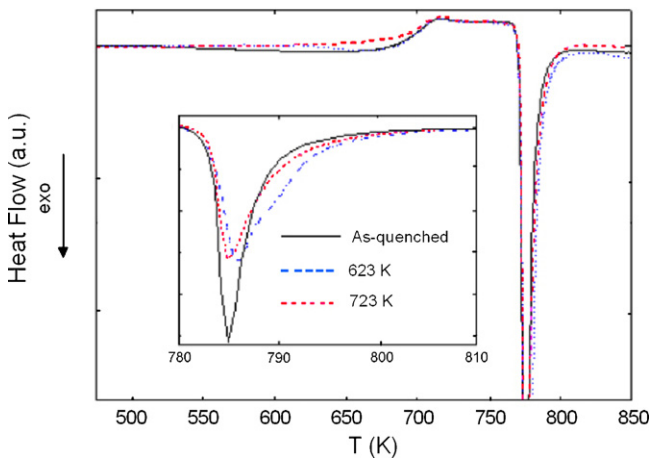

Fig. 3. Differential scanning calorimetry (DSC) curves of the as-quenched $Zr_{55}Cu_{30}Al_{10}Ni_5$ rod before and after annealing to 623 and 723 K. The inset shows an enlargement of the crystallization peaks.

Plastic flow induced by HPT is typically inhomogeneous along the disk radius, with a larger amount of deformation occurring at the edge than in the center of the disk, especially for a low number of revolutions [2]. Deformation at sufficiently low temperatures (below T_g) increases the net amount of free volume, tending to increase the exothermic halo preceding glass transition. As shown in Fig. 2, the relaxation exotherm is indeed more pronounced in the HPT disk (both for the center and the edge of the disk) as compared to the as-cast, undeformed state. However, although free volume increases significantly at the onset of deformation, at a certain moment the amount of excess free volume saturates (when an equilibrium between creation and annihilation is reached) [22] or can even decrease, due to the formation of more stable nanovoids [11,36]. This could explain why in fact the center of the HPT disk, with a lower amount of deformation, shows a more pronounced relaxation exotherm. Contrary to the HPT disks, a clear decrease in the relaxation halo is observed in the annealed samples in comparison with the as-quenched rod (Fig. 3). It has been demonstrated that the relaxation enthalpy is actually proportional to the amount of excess free volume frozen within the amorphous structure of the glass [10]. Upon heating, free volume tends to progressively annihilate, leading to a topologically relaxed structure and the concomitant observed smoothing of the relaxation DSC exotherm. Hence, the interesting point is that, on the one hand, SPD seems to introduce analogous changes in the glassy structure of the rod as low-temperature annealing (resulting in an similar shape of the crystallization peak) while, on the other hand, circumventing the competing adverse effect of thermally induced topological relaxation, which typically leads to embrittlement and premature fracture.

4.2. Microstructural characterization

4.2.1. X-ray diffraction

Investigation by conventional XRD shows the 'Bragg amorphous' nature of the as-quenched, annealed and HPT (whole disk) samples: two broad diffuse halos are observed, without any sharp diffraction peaks typical for the presence of crystalline phases (Fig. 4). The main halos were fit to a pseudo-Voight function. The coherent diffraction domain sizes and microstrains were calculated from the integral peak width of the Lorentzian and Gaussian contributions, respectively. The results, shown in Table 1, indicate that the size of the coherent diffraction domain comes mainly from the medium-range order present in metallic glasses (order scale of 1 nm). In turn, the microstrains accumulated inside the material increase slightly

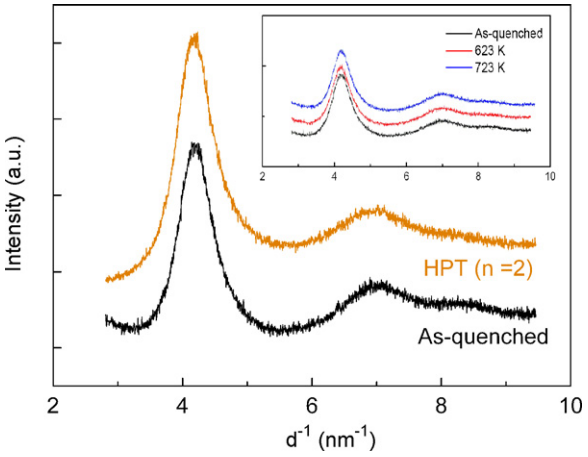

Fig. 4. X-ray diffraction patterns of the $Zr_{55}Cu_{30}Al_{10}Ni_5$ alloy acquired in the as-quenched state and after severe plastic deformation induced by high-pressure torsion (HPT). Shown in the inset are the X-ray diffraction patterns of the same alloy, recorded at room temperature, before and after annealing at 623 and 723 K.

Table 1
Structural parameters (coherent diffraction domain, δ, and root-mean-square microstrains, $\langle\varepsilon^2\rangle^{1/2}$), obtained by fitting the XRD patterns of the as-quenched rod, HPT disk and undeformed samples annealed at 623 and 723 K, using a pseudo-Voigt function. Note that Γ_G and Γ_L represent, respectively, the integral width from the Gaussian and Lorentzian contributions of the pseudo-Voigt function.

	Γ_L	δ (nm)	Γ_G	$\langle\varepsilon^2\rangle^{1/2}$
As-quenched	6.1	1.65	5.4	0.024
HPT disk	6.1	1.65	6.1	0.028
Annealed 623 K	6.1	1.65	5.3	0.024
Annealed 723 K	6.0	1.67	4.9	0.022

after deformation, as expected, whereas thermal annealing leads to structural relaxation, i.e., a decrease of microstrains.

4.2.2. Transmission electron microscopy

As it has been shown in Section 3, HPT introduces not only a large shear strain in the material but also causes a significant temperature increase. In order to shed light into the structural changes induced by severe plastic deformation on the $Zr_{55}Cu_{30}Al_{10}Ni_5$ glassy structure, comparative TEM observations were performed after HPT deformation and after thermal annealing of an undeformed specimen at 623 and 723 K.

Observation by TEM reveals a clear difference in the microstructures of the as-cast and annealed samples (Fig. 5). While the as-cast sample shows a homogeneous, featureless microstructure [(panel (a)], the microstructure of the annealed samples [panels (b) and (c)] consists of a bright matrix with darker regions, with sizes in the order of 5–10 nm. The selected area electron diffraction (SAED) patterns, shown in the respective insets, indicate the conservation of an overall amorphous structure, although the outer rings become each time a bit sharper upon annealing, pointing towards increased ordering, at least at local length scales. More detailed analysis using high angle annular dark field in combination with high-resolution scanning transmission electron microscopy (not shown) revealed that annealing at these temperatures brings about compositional fluctuations, i.e. some regions become richer in Cu than the surrounding matrix [37].

Similar to the annealed $Zr_{55}Cu_{30}Al_{10}Ni_5$ glass, the TEM images obtained after HPT processing do not immediately show any sign of clear deformation-induced crystallization. This is in agreement with the results from DSC, where the crystallization peaks of both heat-treated and deformed specimens are very similar (cf. Figs. 2 and 3). At a first glance, the overall images after SPD, shown in Fig. 6, appear homogeneous and amorphous. Looking into further detail shows the presence of some variations within the microstructure. Indeed, there seem to be elongated zones with different "orientation", repetitively found throughout the whole sample (delimited with discontinuous white lines in the figure). This effect could be caused by thickness variations, but note that they are on the order of 15–20 nm which is unlikely to be caused by sample preparation. Most likely structural variations are caused by the large HPT shear strains and might be related to formation of shear band upon deformation (note that typical shear band thickness is on the order of 20–30 nm [38], thus similar to the regions indicated in Fig. 6). It is worth mentioning that shear bands are likely to form during the first stages of HPT processing, when the temperature rise associated with the shear strain is still rather low. Nevertheless, as temperature during HPT increases, plastic flow will tend to become more homogeneous, in agreement with the deformation map developed by Schuh et al., which predicts a transition from heterogeneous plastic flow (with shear band formation and propagation) to homogeneous deformation (without shear bands) for $T > 0.8T_g$ [8]. Note that indeed the temperature rise during HPT after two whole revolutions is already quite close to T_g (see Fig. 1).

In a second step, the HPT sample was investigated in a high-resolution TEM, equipped with a spherical aberration corrector. This increases resolution significantly [39], and is even capable of revealing medium-range order of metallic glasses [40]. Analysis of the deformed sample reveals presence of two main types of clusters/nanocrystals: both are face-centered cubic (fcc), but with different lattice parameters (Fig. 7). The first type has a lattice parameter of 3.6 Å and most likely corresponds to Cu-rich clusters. This might indicate that the observed changes are similar to the structures induced by low-temperature annealing. The second

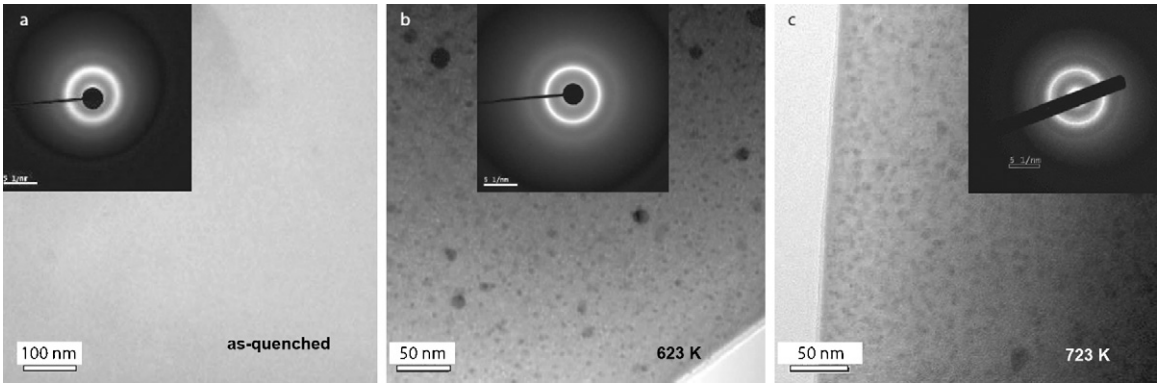

Fig. 5. Microstructural features of the $Zr_{55}Cu_{30}Al_{10}Ni_5$ alloy, observed by transmission electron microscopy, in (a) the as-quenched state, (b) sample annealed to 623 K (sub-T_g annealing) and (c) sample annealed to 723 K (sub-T_x annealing). Shown as insets are the corresponding selected area electron diffraction patterns.

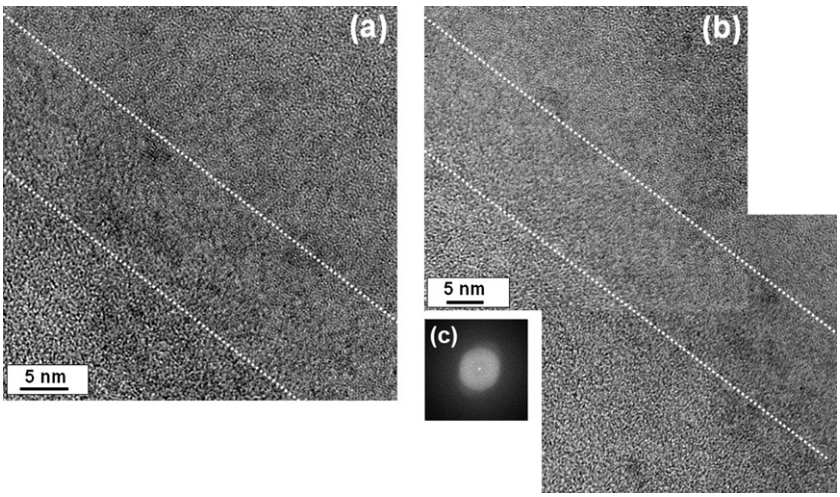

Fig. 6. Transmission electron microscopy images of the $Zr_{55}Cu_{30}Al_{10}Ni_5$ alloy processed by high-pressure torsion [panels (a) and (b)]. The dashed white lines indicate regions where variations in the amorphous structure can be observed. Panel (c) is the Fourier transform of image (a).

type of cluster has a lattice parameter of 5–5.2 Å. This could be ZrO_2 (*Fm*3*m* with cell parameter 5.07 Å) but no increase in the oxygen signal was detected by electron energy loss spectroscopy (EELS) as compared to the matrix (within the sensibility of this technique, which is around 1%). Another possibility could be that these clusters are the building blocks of the medium-range order of the amorphous material in general [41]. Note that 2.9 Å is on one hand the closest packed direction in these fcc-clusters and is also the distance where the main halo appears in the electron diffraction pattern of the amorphous material. It should be noted that the latter type of clusters was also occasionally detected by the same technique in the undeformed material (not shown).

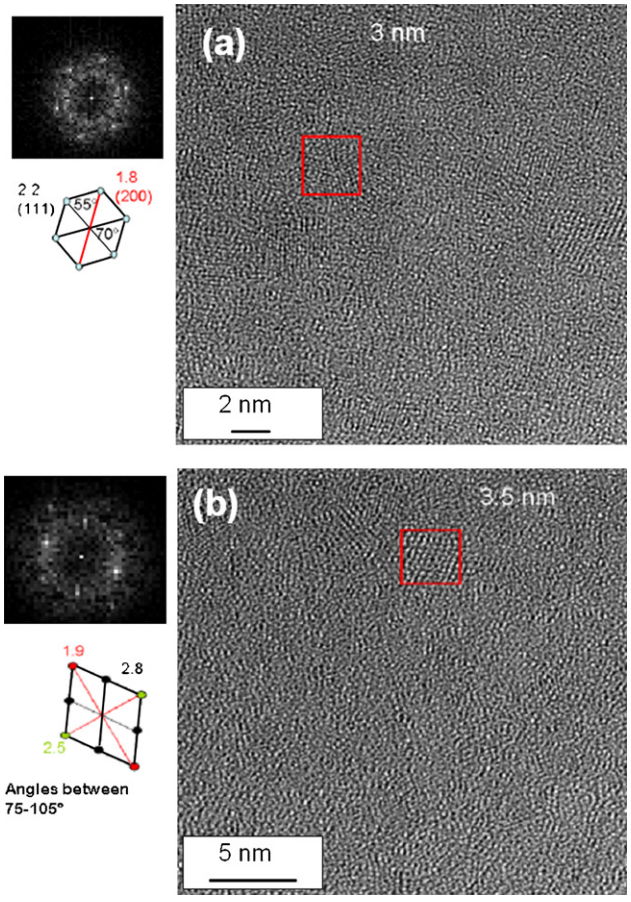

Fig. 7. Analysis of the clusters/nanocrystals in the sample deformed by high-pressure torsion by high-resolution transmission electron microscopy with a C_s corrector. Two main clusters have been analyzed: (a) Cu-like clusters and (b) an fcc-type cluster with lattice parameter around 5–5.2 Å.

It should be noted that in spite of the lack of long-range order, metallic glasses do, however, exhibit a short-range order. This short-range order is the consequence of the attractive interactions between the atoms forming the MG. These interactions lead to the formation of clusters, where solute atoms are surrounded by atoms of a more numerous species. The way these atomic clusters interconnect to fill the 3D space leads to the concept of medium-range order. Recent models have suggested that the medium-range order is the result of fcc, icosahedral five-fold and even more complex arrangements of neighboring atomic clusters [42–44]. Cs-corrected transmission electron microscopy allows observing medium-range order in metallic glasses [40] and our results suggest that in this particular alloy the medium-range order may follow the fcc symmetry.

4.3. Mechanical characterization using nanoindentation

Crystalline materials deformed/processed by HPT can show quite inhomogeneous microstructures and a gradient in mechanical properties as a function of the position along the disk radius, with the finest microstructure and the highest hardness observed at the edge. The effect of a possible inhomogeneous stress distribution along the radius of the investigated glassy rod has been investigated by nanoindentation. The results have been compared with those obtained on as-quenched and heat-treated glassy specimens.

When contrasting the indentation curves of as-quenched and HPT samples, the main difference is that the deformed sample shows reduced shear band activity. Indeed, a decrease in the pop-in events or serrations is observed in the load-displacement curve after deformation, particularly for low applied loads (Fig. 8). Note that this effect can only be investigated through indentation experiments at sufficiently low loads, when the problem of lack of resolution is circumvented. Our results are in agreement with those reported by Jiang and Atzmon [16] and Tang [45], who also observed a reduced amount of shear banding/pileup and/or a reduced amount of serrations in the load-displacement indentation curves of previously deformed specimens. These observations can be explained by considering the interplay between nucleation of new shear bands and propagation of pre-existing ones. While clear serrations in the loading curves of undeformed sample indicate that

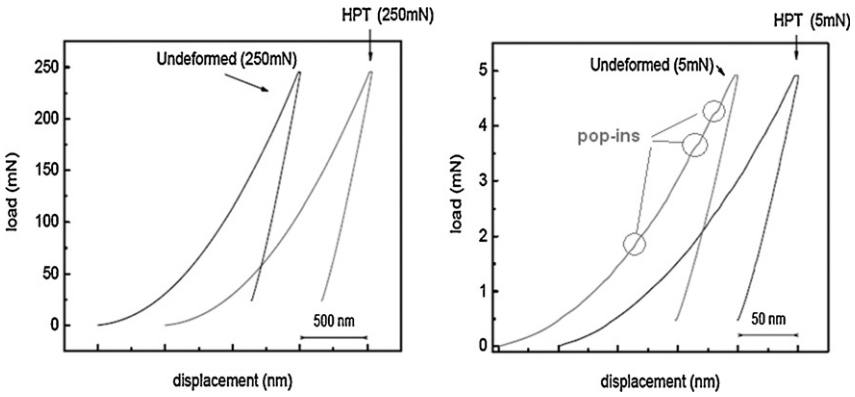

Fig. 8. Load–displacement nanoindentation curves of the undeformed $Zr_{55}Cu_{30}Al_{10}Ni_5$ sample and a disk processed by high-pressure torsion. The curves in (a) were obtained using a maximum load of 250 mN, whereas (b) shows nanoindentation curves with higher resolution, obtained with a maximum load of 5 mN. Note that serrations (or pop-ins events) can be clearly seen in (b), particularly for the undeformed sample.

during nanoindentation the main deformation mechanism is the nucleation and propagation of new shear bands, in the deformed sample the predominant deformation mechanism during nanoindentation is likely to be the propagation of pre-existing shear bands, developed during the prior high-pressure torsion processing.

Fig. 8 also shows that the maximum penetration depth achieved at the end of the loading segments of the indentation curves is larger for the HPT disk than for the as-quenched rod. This suggests the occurrence of a mechanical softening during SPD, in spite of the deformation-induced heating of the sample, which would a priori favor an increase of hardness. The values of hardness, calculated from indentation curves with a maximum applied load of 250 mN, are plotted in Fig. 9 as a function of the position along the radius of the HPT disk. A moderate softening indeed occurs upon deformation, as compared to the undeformed sample, which is in accordance with the observed increase in free volume (Fig. 2). A similar decrease was observed in the reduced Young's modulus (Fig. 10), which could be also due to an increase in free volume and the concomitant increase in interatomic spacing. However, the altered medium-range order, with formation of Cu-clusters (Fig. 7), might be a second effect contributing to the observed hardness and modulus decrease. It is worth mentioning that the hardness values of the samples heat-treated to 623 and 723 K are 6.9 and 6.6 GPa, respectively, thus larger than for the as-quenched rod (and HPT specimens). This is probably due to the structural relaxation (and consequent decrease of free volume) that occurs during

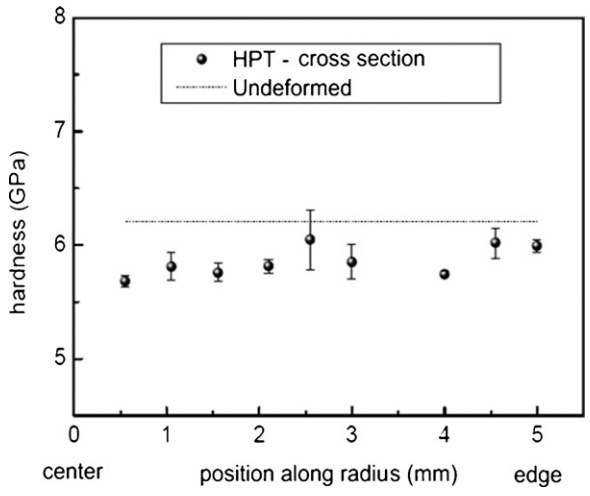

Fig. 9. Dependence of hardness on the position along the HPT disk radius, measured along the cross-section of the disk. Indicated with a dashed line is the hardness value of the undeformed sample.

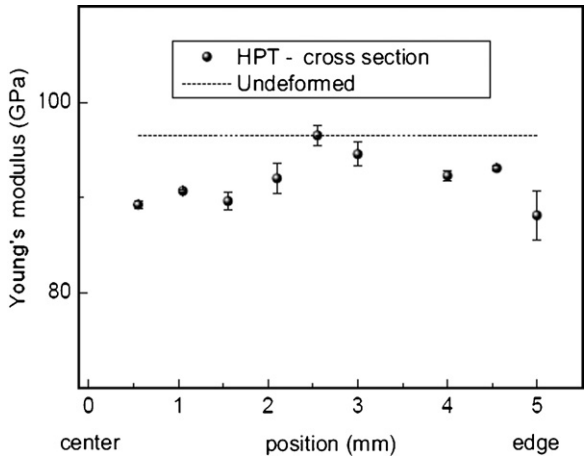

Fig. 10. Dependence of the reduced Young's modulus on the position along the HPT disk radius, measured along the cross-section of the disk. Indicated with a dashed line is the Young's modulus value of the undeformed sample.

thermal annealing, as evidenced by DSC (Fig. 3). Our hardness measurements indicate that although local heating accompanying HPT would tend to increase the hardness (as a result of free volume annihilation), the shear strains during SPD are so high that the newly created free volume during deformation overcomes the thermally annihilated one, thus causing an overall softening effect. Finally, no large differences are seen between edge and center of each sample, except for a slight increase in hardness towards the edge of the HPT disk. This is interesting since it indicates that deformation in the whole disk is more or less homogeneous, contrary to what it usually occurs in crystalline metals, hence reinforcing the possible use of HPT as a method to produce bulky uniform amorphous samples.

5. Conclusions

Severe plastic deformation of $Zr_{55}Cu_{30}Al_{10}Ni_5$ bulk metallic glass induces an increase in the amount of free volume (i.e., dilatation) and formation of nanoclusters with modified medium-range order. Conversely, thermal annealing (without deformation) of the as-quenched $Zr_{55}Cu_{30}Al_{10}Ni_5$ rods induces a reduction of free volume (i.e., densification) and fluctuations in the chemical ordering, both of which occur simultaneously. Hence, although HPT produces a local temperature rise in the material being deformed (bringing it close to the glass transition), the microstructural modifications observed after heavy deformation are mainly ascribed

to the large shear strains, which overcome thermal effects. The observed mechanical softening after HPT is, on the other hand, rather moderate and it occurs quite homogeneously throughout the processed disk, indicating that deformation is certainly a treatment with promising potential to manufacture bulky glassy specimens with enhanced atomic mobility and uniform properties.

Acknowledgements

Partial financial support from the Catalan DURSI (2009-SGR-1292 research project) and the Spanish Ministry of Science and Innovation (MAT 2007-61629 project) is acknowledged. We also thank the *Servei de Microscopia* of the *Universitat Autònoma de Barcelona* for the technical assistance during electron microscopy observations. TEM experiments in Toulouse were supported by the ESTEEM European project. Á.R. is indebted for the Bolyai Scholarship of the Hungarian Academy of Sciences. We appreciate the support of the Hungarian Research Fund (OTKA) under Grant No.: F67893. M.D.B. was partially supported by an ICREA ACADEMIA award.

References

[1] G.E. Dieter, Mechanical Metallurgy, 3rd ed., McGraw-Hill, New York, 1986.
[2] A.P. Zhilyaev, G.V. Nurislamova, B.K. Kim, M.D. Baró, J.A. Szpunar, T.G. Langdon, Acta Mater. 51 (2003) 753–765.
[3] N. Boucharat, R.J. Hebert, H. Rösner, G. Wilde, Solid State Phenom. 114 (2006) 123–132.
[4] J. Sort, D.C. Ile, A.P. Zhilyaev, A. Concustell, T. Czeppe, M. Stoica, S. Suriñach, J. Eckert, M.D. Baró, Scripta Mater. 50 (2004) 1221–1225.
[5] Zs. Kovács, P. Henits, A.P. Zhilyaev, Á. Révész, Scripta Mater. 54 (2006) 1733–1737.
[6] Á. Révész, J.L. Lábár, S. Hóbor, A.P. Zhilyaev, Zs. Kovács, J. Appl. Phys. 100 (2006) 103522.
[7] A. Révész, E. Schafler, Zs. Kovács, Appl. Phys. Lett. 92 (2008) 011910.
[8] C. Schuh, T. Hufnagel, U. Ramamurty, Acta Mater. 55 (2007) 4067–4109.
[9] D.V. Louzguine, A.R. Yavari, K. Ota, G. Vaughan, A. Inoue, J. Non-Cryst. Solids 351 (2005) 1639–1645.
[10] A. Slipenyuk, J. Eckert, Scripta Mater. 50 (2004) 39–44.
[11] K.M. Flores, E. Sherer, A. Bharathula, H. Chen, Y.C. Jean, Acta Mater. 55 (2007) 3403–3411.
[12] B.P. Kanungo, S.C. Glade, P. Asoka-Kumar, K.M. Flores, Intermetallics 12 (2004) 1073–1080.
[13] N. Van Steenberge, J. Sort, A. Concustell, J. Das, S. Scudino, S. Suriñach, J. Eckert, M.D. Baró, Scripta Mater. 56 (2007) 605–608.
[14] J. Fornell, A. Concustell, S. Suriñach, W.H. Li, N. Cuadrado, A. Gebert, M.D. Baró, J. Sort, Int. J. Plast. 25 (2009) 1540–1559.
[15] Y. Deng, L. He, Q. Zhang, H. Zhang, H. Ye, Adv. Eng. Mater. 5 (2003) 738–741.
[16] W.H. Jiang, F.E. Pinkerton, M. Atzmon, Acta Mater. 53 (2005) 3469–3477.
[17] M. Chen, A. Inoue, W. Zhang, T. Sakurai, Phys. Rev. Lett. 96 (2006) 245502.
[18] J.J. Kim, Y. Choi, S. Suresh, A.S. Argon, Science 295 (2002) 654–657.
[19] J. Fornell, E. Rossinyol, S. Suriñach, M.D. Baró, W.H. Li, J. Sort, Scripta Mater. 62 (2010) 13–16.
[20] S.W. Lee, M.Y. Huh, E. Fleury, J.C. Lee, Acta Mater. 54 (2006) 349–355.
[21] P. Henits, A. Révész, A.P. Zhilyaev, Zs. Kovács, J. Alloys Compd. 461 (2008) 195–199.
[22] Q. Cao, J. Li, Y. Zhou, J. Jiang, Appl. Phys. Lett. 86 (2005) 081913.
[23] J. Das, K.B. Kim, W. Xu, B.C. Wei, Z.F. Zhang, W.H. Wang, S. Yi, J. Eckert, Mater. Trans. 47 (2006) 2606–2609.
[24] L. Liu, Q. Chen, K.C. Chan, J.F. Wang, G.K.H. Pang, Mater. Sci. Eng. A 449–451 (2007) 949–953.
[25] T.G. Nieh, J. Wadsworth, C.T. Liu, T. Ohkubo, Y. Hirotsu, Acta Mater. 49 (2001) 2887–2896.
[26] Q. Cao, J.F. Li, Y. Hu, A. Horsewell, J.Z. Jiang, Y.H. Zhou, Mater. Sci. Eng. A 457 (2007) 94–99.
[27] Y. Zhang, W.H. Wang, A.L. Greer, Nat. Mater. 5 (2006) 857–860.
[28] J.J. Lewandowski, A.L. Greer, Nat. Mater. 5 (2006) 15–18.
[29] L. Battezzati, G.M. Morarino, J. Alloys Compd. 483 (2009) 222–226.
[30] M.D. Demetriou, W.L. Johnson, Acta Mater. 52 (2004) 3403–3412.
[31] W.H. Jiang, M. Atzmon, Acta Mater. 51 (2003) 4095–4105.
[32] W.C. Oliver, G.M. Pharr, J. Mater. Res. 7 (1992) 1564–1583.
[33] S. Hóbor, Zs. Kovács Zs, A. Révész, J. Appl. Phys. 106 (2009) 023531.
[34] G.S. Fulcher, J. Am. Ceram. Soc. 8 (1925) 339–355.
[35] R.Z. Valiev, R.K. Islamgaliev, I.V. Alexandrov, Prog. Mater. Sci. 45 (2000) 103–189.
[36] K.M. Flores, Scripta Mater. 54 (2006) 327–332.
[37] N. Van Steenberge, A. Concustell, J. Sort, J. Das, N. Mattern, A. Gebert, S. Suriñach, J. Eckert, M.D. Baró, Mater. Sci. Eng. A 491 (2008) 124–130.
[38] Y. Zhang, A.L. Greer, Appl. Phys. Lett. 89 (2006) 281633.
[39] B. Freitag, S. Kujawa, P.M. Mul, J. Ringalda, P.C. Tiemeijer, Ultramicroscopy 102 (2005) 209–214.
[40] A. Hirata, Y. Hirotsua, T.G. Nieh, T. Ohkuboc, N. Tanaka, Ultramicroscopy 107 (2007) 116–123.
[41] A. Guinier, X-ray Diffraction in Crystals, Imperfect Crystals and Amorphous Bodies, General Publishing Company, Ltd, Toronto, 1994.
[42] D.B. Miracle, Nat. Mater. 3 (2004) 697–702.
[43] H.W. Sheng, W.K. Luo, F.M. Alamgir, J.M. Bai, E. Ma, Nature 439 (2006) 419–425.
[44] C. Fan, P.K. Liaw, T.W. Wilson, W. Dmowski, H. Choo, C.T. Liu, J.W. Richardson, Th. Proffen, Appl. Phys. Lett. 89 (2006) 111905.
[45] C. Tang, Y. Li, K. Zeng, Mater. Sci. Eng. A 384 (2004) 215–223.